From the Bulk to the Nanoscale: Strong Evolution in the Structure and Chiroptical Properties of Chiral Halide Double Perovskites

Maria Maniadi, Kostiantyn Tieriekhov, Olivier Ségut, Nicolas Mercier, Alexandre Abhervé

ADVANCED OPTICAL MATERIALS
www.advopticalmat.de

From the Bulk to the Nanoscale: Strong Evolution in the Structure and Chiroptical Properties of Chiral Halide Double Perovskites

*Maria Maniadi, Kostiantyn Tieriekhov, Olivier Ségut, Nicolas Mercier, and Alexandre Abhervé**

In the quest for lead-free chiral metal-halide materials, 2D double perovskites appear as very promising candidates especially for spintronic applications. However, compared to highly crystalline Pb^{2+} compounds, the more challenging synthetic procedure for compounds based on Ag^{+} and Bi^{3+}/Sb^{3+} so far limited the number of these chiral materials to very few reported examples, as highlighted by the absence of crystal structure based on the extensively used (*S*/*R*)-1-phenylethylammonium (*S*/*R*-MBA) cations in chiral metal halides. This study presents the successful preparation and characterization of a complete series of 2D bromide-based and iodide-based double perovskites based on the cations (*S*/*R*)-1-(4-bromophenyl)ethylammonium (*S*/*R*-4BrMBA), which allows to describe their structures, thin film processing, and resulting chiroptical properties. The strong modulation of the structure and circular dichroism (CD) properties at the nanoscale is unprecedented, since the thin films of (*S*/*R*-4BrMBA)$_4$AgBiBr$_8$ strongly evolve from a single-phase compound with small intrinsic CD_{iso} to a polymorphic material showing a strong increase in the CD signal due to macroscopic effects.

1. Introduction

Chiro-spintronics is an emergent field of research since the ability of chiral materials to create polarized light and/or electric current has been discovered.[1] Chiral halide perovskites have appeared as relevant materials in this field, thanks to their intrinsic optoelectronic properties and the possibility to use chiral organic cations in hybrid organic-inorganic structures.[2] In the last seven years, much effort has been dedicated to the synthesis and chiral properties characterization of chiral halide perovskites based on Pb^{2+}.[3] Indeed, 2D or 1D lead-based materials were easily prepared starting from commercially available chiral amines such as (*S*/*R*)-1-phenylethylamine (abbreviated as *S*/*R*-MBA in their cationic form) and PbX_2 salts (X = Cl, Br, I).[4] The representative examples with formula (*S*/*R*-MBA)PbX_4 have been extensively studied and confirmed the potential of low-dimensional halide perovskites for applications in non-linear optics (such as the light-polarization-dependent second-harmonic generation, SHG-CD),[5] circularly polarized luminescence (CPL)[6] and spintronic devices such as CPL detectors[7] and spin-light-emitting devices (spin-LEDs).[8] Particularly, (*S*/*R*-MBA)PbI_4 revealed a strong ability for the creation of spin-polarized currents, a phenomenon called CISS effect (chirality-induced spin selectivity).[9] The fundamental origins of such a strong spin-polarization ability are still a mystery, requiring a systematic study on a large series of compounds.[10] In this context, lead-free materials are promising for both practical applications and to disclose the role of the metal ion in the chiro-spintronic properties. So far, few examples of tin-based compounds have been investigated,[11] although such compounds can be difficult to handle due to the easy oxidation of Sn^{2+} into Sn^{4+}.[12] Another strategy consists in the replacement of Pb^{2+} by alternating Ag^{+} and Bi^{3+} or Sb^{3+}, leading to the so-called family of halide double perovskites. However, such heterometallic compounds are more difficult to crystallize, as confirmed by the absence of (*S*/*R*-MBA)$_4$AgBiX_8 compounds in the literature. As a matter of fact, only four examples of chiral halide double perovskites have been reported to date,[13–16] due to the difficulty of adapting the synthetic strategy. Nevertheless, it remains critical to prepare lead-free halide double perovskite materials, especially for the fundamental understanding of the structural parameters governing the chiroptical and spintronic performances. Recently, para-substituted *S*/*R*-XMBA, such as (*S*/*R*)-1-(4-bromophenyl)ethylammonium (*S*/*R*-4BrMBA), were described as suitable cations to enhance the spin splitting in 2D halide perovskites, a strategy to improve the CISS effect.[17] These cations have thus been used to prepare 2D lead-based compounds with interesting circular dichroism (CD), CPL, and

M. Maniadi, K. Tieriekhov, O. Ségut, N. Mercier, A. Abhervé
MOLTECH-Anjou, UMR 6200, CNRS
UNIV Angers, 2 bd Lavoisier, ANGERS Cedex 49045, France
E-mail: alexandre.abherve@univ-angers.fr

The ORCID identification number(s) for the author(s) of this article can be found under https://doi.org/10.1002/adom.202402949

DOI: 10.1002/adom.202402949

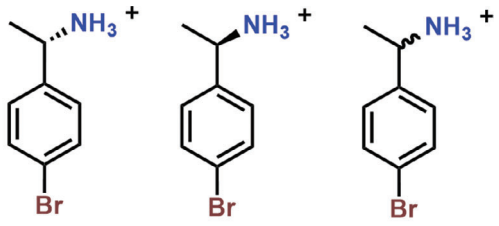

Scheme 1. Structure of the cations used in this work.

circular photogalvanic properties.[18–21] In this work, we have used *S*/*R*-4BrMBA cations to prepare a unique series of chiral halide double perovskites (**Scheme 1**). Contrary to *S*/*R*-MBA cations which could only give rise to discrete species of formula $(S/R\text{-MBA})_2BiX_5$[22–23] or 1D networks of formula $(S/R\text{-MBA})BiI_4$,[24] the family of compounds of general formula $(S/R\text{-4BrMBA})_4AgBiX_8$ (X = Br or I) show the typical 2D perovskite network of corner-sharing octahedra with alternating Ag^+ and Bi^{3+} metal ions. Interestingly, the bromide-based double perovskites exhibit multiple crystal phases of different symmetries, as observed with one triclinic phase and one orthorhombic phase in the bulk, while one more phase could be detected in the film state. Even more intriguing, the evolution of these phases inside the thin films could be observed by X-ray powder diffraction (XRPD). This evolution is accompanied by a strong evolution in the CD response of the thin films, giving rise to the macroscopic circular absorption called aLDLB. On the other hand, strong CD signals were observed in $(S/R\text{-4BrMBA})_4AgBiI_8$ thin films due to the presence of both intrinsic thickness-independent CD and macroscopic thickness-dependent effects.

2. Results and Discussion

2.1. Synthesis and Crystal Structures

The crystallization of chiral halide double perovskites required an adapted synthetic procedure based on the slow evaporation method. The synthesis of the bromide-based compounds used stoichiometric ratio between $AgNO_3$ and $BiBr_3$, by dissolving first $AgNO_3$ in HBr upon heating at 200 °C until a clear yellow solution was obtained. After a few minutes a dark red solution was obtained due to the partial oxidation of Br^- to Br_2 induced by $AgNO_3$. In order to reduce Br_2 into Br^-, a few drops of H_3PO_2 acid were needed. $BiBr_3$ was added to the resulting yellow solution and after complete dissolution the temperature was lowered to 150 °C. After addition of the amine, the reaction mixture was heated for 15 min and left to cool down to ambient temperature, until small yellow plate-like crystals of polymorphs 1*S* and 1*R* precipitated. In order to obtain polymorphs 2*S* and 2*R*, small amounts of crystals of 1*S* and 1*R* were placed in an oven at 120 °C for 30 min. For the synthesis of the iodide-based compounds, an excess amount of $AgNO_3$ was used in order to avoid any bismuth-based byproducts. Non-stoichiometric amounts of $AgNO_3$ and $Bi(NO_3)_3{\cdot}5H_2O$ were dissolved in HI upon heating at 120 °C until a dark red solution was obtained. The amine was dissolved in H_3PO_2 solution at room temperature and added to the reaction mixture giving a clear red solution. A slow cooling down with a step at 60 °C for ≈6 h allowed to improve the quality of the precipitated crystals. It is important to note that replacing the S/R-4BrMBA precursor by *R*-MBA in the same synthetic conditions could only afford crystals of the already reported 0D compound of formula $(R\text{-MBA})_2BiX_5$ (Figure S1, Supporting Information).[22,23] Therefore, both the choice of the cation and of the synthetic conditions here described were critical to crystallize the 2D halide perovskite networks. Single-crystal X-ray diffraction could be performed on both polymorphs of bromide and iodide-based compounds (Tables S1–S6, Supporting Information). The first polymorphs of $(S/R\text{-4BrMBA})_4AgBiBr_8$ (1*S* and 1*R*) crystallized in the triclinic *P*1 space group and present in the asymmetric unit eight independent organic molecules and four independent octahedra of alternating Bi1, Ag1 and Bi2, Ag2 (Figure S2, Supporting Information). The 2D network of corner-sharing octahedra expand along the (110) crystallographic plane, with two distinct layers in the unit cell (**Figure 1a**). These layers are stabilized by the orientation of the cations with the ammonium heads pointing toward the inorganic part. As a result, strong in-plane distortions appear as highlighted by the distortion indices[25] of 0.03195-0.03297 for $BiBr_6$ octahedra and 0.11518-0.11823 for $AgBr_6$ octahedra. Indeed, equatorial Bi–Br and Ag–Br bond lengths span in the range of 2.7668(6)-2.9787(7) and 2.5118(6)-3.5369(40) Å, respectively, and axial bond lengths are between 2.7623(5)-2.9723(5) and 3.0323(5)-3.5332(6) Å, respectively (Figure S3, Supporting Information). On the other hand, Bi–Br–Ag bond angles show rather small deviation as highlighted by the range of 148.937(6)-160.634(6)° (Figure S4, Supporting Information). Regarding the organic part, two distinct layers were observed, the first one being composed of well-oriented molecules and the second one bearing "bending" organic molecules. Indeed, the former one consists of two sets of organic molecules stabilizing each other due to π–Br interactions with values of 3.5202(36) and 3.5893(38)Å, thus revealing the critical role of the bromide substituent on the phenyl ring of the cation for the stabilization of the perovskite network (Figure 1b). On the other hand, the second layer contains four organic molecules with numerous interactions between each other (Figure S5, Supporting Information). π–H interactions are formed either between phenyl groups or between methyl and phenyl groups, while H–Br bonding occur involving aromatic hydrogens. On the other hand, the second polymorphs of $(S/R\text{-4BrMBA})_4AgBiBr_8$ (2*S* and 2*R*) crystallized in the $P2_12_12_1$ space group. Although the asymmetric unit also consists in eight independent organic molecules and four independent octahedra (Figure S6, Supporting Information), only one pair of distinct organic and inorganic layers could be observed in the unit cell (Figure 1c). The inorganic layer of alternating Bi1-Ag1-Bi2-Ag2 thus adopts a wavy periodicity along the (101) crystallographic plane (Figure 1b). $AgBr_6$ octahedra show stronger distortion than those of the triclinic phase as highlighted by the distortion indices (0.12761-0.13933) and the Ag–Br bond distance values range between 2.4636(34)-3.7235(25) Å for equatorial bonds and 3.3128(25)-3.7123(30) Å for axial bonds (Figure 1d). As a result, a much higher deviation for the Bi–Br–Ag bond angles can be observed with a range of 151.172(66)-172.944(84)° (Figure S7, Supporting Information). The 2D organic layer consists of five pairs of cations. Four of them are stabilized via π–Br interactions (with intermolecular distances in the

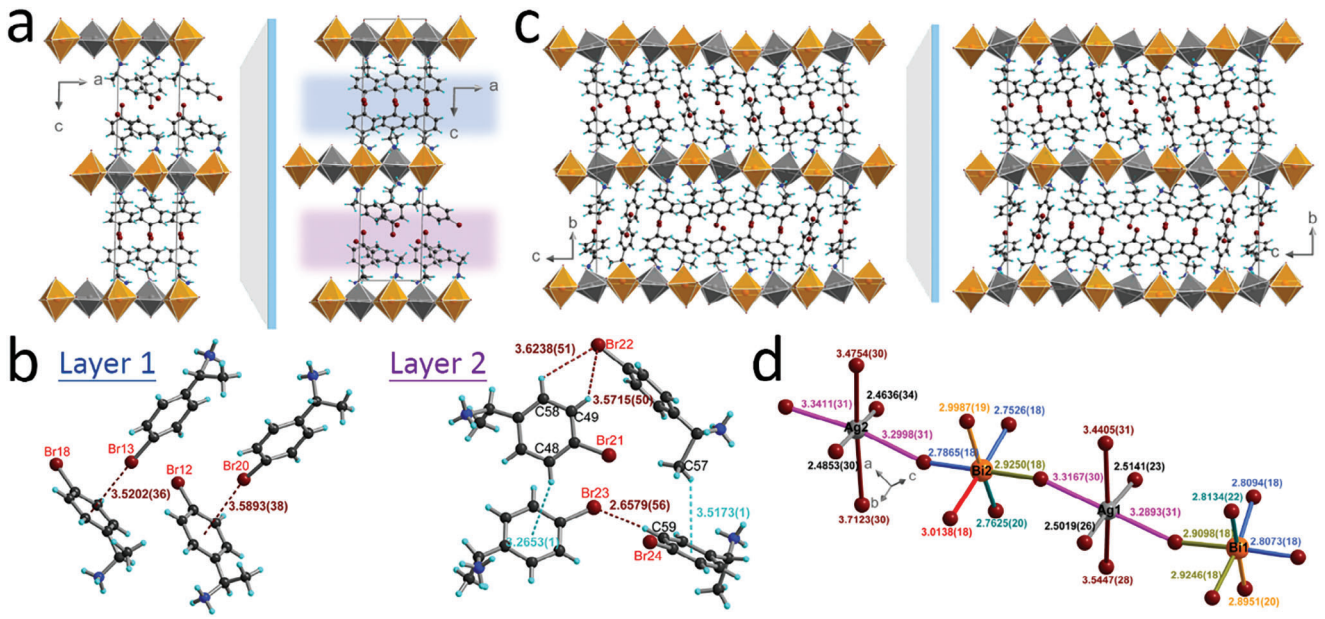

Figure 1. Crystal structures of the two polymorphs of $(S/R\text{-4BrMBA})_4AgBiBr_8$. a) View of the structures of 1*S* and 1*R* (triclinic phase) along the *b* direction, highlighting the two different organic layers in blue and purple. b) Intermolecular interactions between organic cations in the two layers. c) View of the structures of 2*S* and 2*R* (orthorhombic phase) along the *a* direction. d) Distortion of the $BiBr_6$ and $AgBr_6$ octahedra in the asymmetric unit of 2*S*. Color code: C (black), H (cyan), N (blue), Br (brown), Bi (orange), Ag (dark grey), $BiBr_6$ unit (orange octahedra), $AgBr_6$ unit (grey octahedra). The longest and shortest apical M–Br (M = Bi, Ag) distances are represented in gold and brown, respectively. In (d), all bonds are represented in different colors to highlight the distortion of the inorganic network.

range of 3.6943(19)-3.8082(27) Å), the fifth one showing H_{Ar}–Br bonding of 3.2090(18)-3.5685(18) Å (Figure S8, Supporting Information).

Finally, $(S/R\text{-4BrMBA})_4AgBiI_8$ crystallized in the triclinic *P*1 space group with four independent cations and two alternating Bi and Ag octahedra in the asymmetric unit (Figure S9, Supporting Information), therefore the unit cell is made of only one pair of organic and inorganic layers (**Figure 2**a). The structural distortion is similar to the one observed in the triclinic phase of the bromide-based networks, with distortion indices of 0.03204 for Bi and 0.11114 for Ag. Equatorial Bi–I and Ag–I bond lengths span in the range of 3.0191(24)-3.2174(2) and 3.2442(2)-3.7923(51) Å, respectively, and axial bond lengths are between 2.8894(3)-3.1787(31) and 2.5940(2)-2.7572(41) Å, respectively (Figure S10, Supporting Information). In addition, the Bi–I–Ag bond angles stay in the range of 152.388(4)- 157.952(4)° (Figure 2b). In the organic layer, numerous hydrogen-bonding interactions can be observed between cations, as well as some head-to-tail organizations involving π–Br interactions (Figure S11, Supporting Information).

2.2. Thermal Analysis of the Bulk Materials

The purity of both compounds and polymorphs was confirmed by XRPD. For the triclinic phase of the 2D bromide perovskites, a strong characteristic peak at $2\theta = 5.0°$ can be observed, corresponding to the (002) plane, as well as a relatively small peak at $2\theta = 7.8°$ corresponding to the (003) plane and an intense peak at $2\theta = 10.4°$ corresponding to the (004) plane, indicating the preferential orientation of the polycrystalline sample (Figure S12, Supporting Information). For the orthorhombic phase obtained by heating a sample of the triclinic phase at 120 °C for 30 min, the strong peak at $2\theta = 5.5°$ corresponds to the (020) plane, while the two relatively weak peaks at $2\theta = 8.7°$ and $2\theta = 10°$ correspond to the (031) and (110) planes, respectively (Figure S13, Supporting Information). An intense peak also appears at $2\theta = 11.1°$ corresponding to the (120) plane. The variety of (hkl) to this structure indicate the lack of preferential orientation of the sample. For the 2D iodide compounds, the first peak appears around $2\theta = 5.5°$, corresponding to the (001) plane (Figure S14, Supporting Information). A more intense peak appears around $2\theta = 11.1°$ along with a smaller peak around $2\theta = 13.7°$, corresponding to the (002) and (110) planes, respectively. To estimate the thermal stability of the materials, thermogravimetric analysis (TGA) and differential scanning calorimetry (DSC) experiments were performed on all 2D hybrid materials, in order to reveal potential phase transitions in the range between −10 and 160 °C (Figures S15 and S16, Supporting Information). TGA measurements showed that the decomposition starts at 250 °C and 230 °C in $(S/R\text{-4BrMBA})_4AgBiBr_8$ and $(S/R\text{-4BrMBA})_4AgBiI_8$, respectively, displaying a significant mass loss due to the evaporation of the organic part and the corresponding BiX_3 (X = Br^-, I^-). The mass loss of 89.53% ($(S/R\text{-4BrMBA})_4AgBiBr_8$) and 88.53% ($(S/R\text{-4BrMBA})_4AgBiI_8$) corresponds to ≈4 ($S/R$-4BrMBA), ≈4 HX and ≈1 BiX_3 per formula unit. A 10.66% and 11.47% mass loss, corresponding to ≈1 AgBr, is observed at ≈774 °C and ≈715 °C for $(S/R\text{-4BrMBA})_4AgBiBr_8$ and $(S/R\text{-4BrMBA})_4AgBiI_8$, respectively. DSC measurements on $(S/R\text{-4BrMBA})_4AgBiBr_8$ revealed an irreversible phase transition between triclinic and orthorhombic phases, with the maximum of the strong endothermic peak being at ≈150 °C. On the other hand, the iodide-based compounds do not exhibit any phase transition.

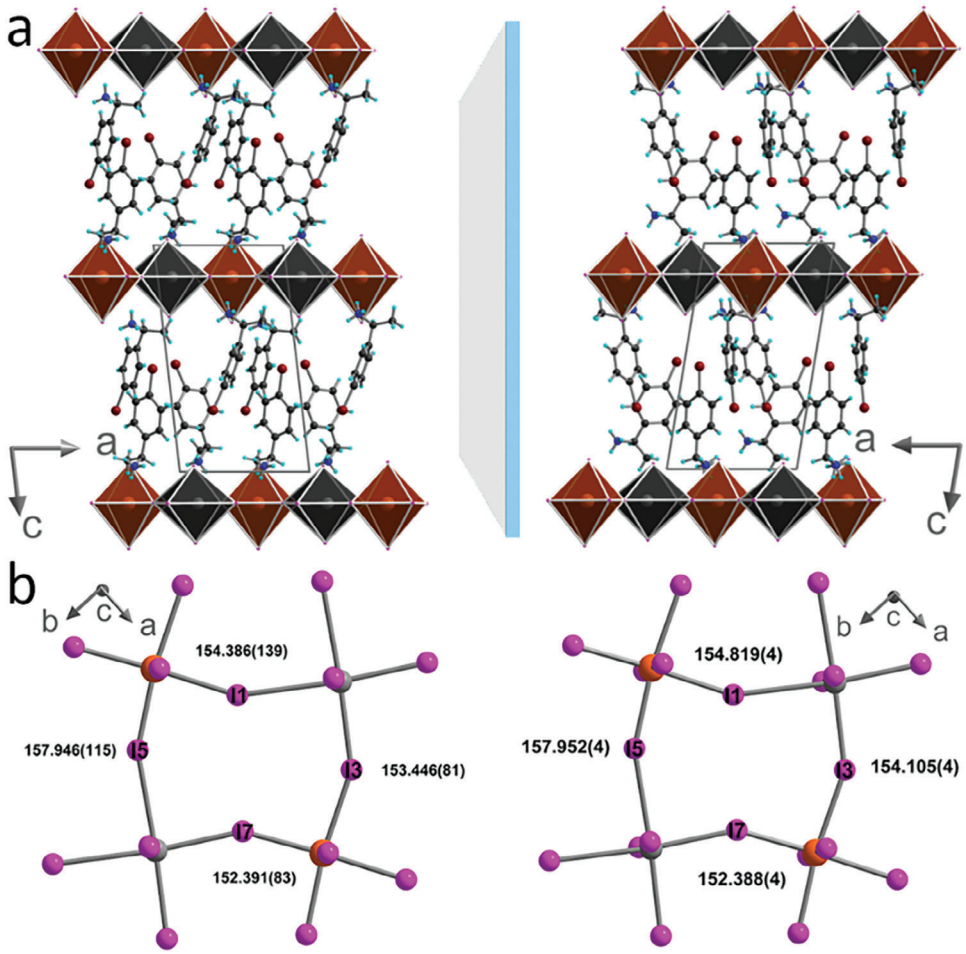

Figure 2. Crystal structures of (*S*/*R*-4BrMBA)$_4$AgBiI$_8$. a) View of the structures of (*S*-4BrMBA)$_4$AgBiI$_8$ (left) and (*R*-4BrMBA)$_4$AgBiI$_8$ (right) along the *b* direction. b) In-plane distortions with bond angles values between BiI$_6$ and AgI$_6$ octahedra. Color code: C (black), H (cyan), N (blue), Br (brown), I (pink), Bi (orange), Ag (dark grey), BiI$_6$ unit (dark orange octahedra), AgI$_6$ unit (dark grey octahedra).

2.3. Processing and Structural Analysis of the Thin Films

Since (*S*/*R*-4BrMBA)$_4$AgBiBr$_8$ compounds undergo a thermally-activated phase transition in the bulk state, it is critical to analyze the nature of the hybrid network in the thin films, especially since an annealing step in the fabrication procedure is required. A polycrystalline sample corresponding to the triclinic phase was first dissolved in anhydrous dimethylformamide (DMF). A series of spin-coated thin films were prepared starting from solutions of various concentrations, from 0.1 to 0.5 M based on the formula unit. Subsequent XRPD measurements revealed that the thin films show strong diffraction peaks at 5.69 and 11.38° which are not indexed in either the triclinic or orthorhombic unit cells (**Figure 3a**; Figure S17, Supporting Information). However, all peaks can be indexed in the same family of (hkl) planes, confirming that the films are based on a single-phase compound. Next, measuring the diffractograms after one day revealed the appearance of new peaks corresponding to the (002) and (004) planes from the triclinic phase 1*S*/1*R* (5.23 and 10.46°) and the (020) and (040) planes from the orthorhombic phase 2*S*/2*R* (5.46 and 10.92°, see Figure S18, Supporting Information). These results first confirmed that the phase observed in the fresh films must correspond to a compound with similar chemical composition (i.e., containing both Ag^+ and Bi^{3+} metal ions), and very probably to a 2D double perovskite compound. Indeed, the first peaks observed at 5.69 and 11.38° might be attributed to (hkl) planes corresponding to the stacking of the 2D layers in a third polymorph of (*S*/*R*-4BrMBA)$_4$AgBiBr$_8$, hereafter named 3*S*/3*R*. This is also strongly supported by the UV–vis absorption spectra of the fresh films (vide infra). In the light of these surprising results, a precise time-resolved analysis on the evolution of the films has been undertaken (Figure 3a; Figure S19, Supporting Information). This study revealed that for (*R*-4BrMBA)$_4$AgBiBr$_8$, the relative intensity of the peaks corresponding to 3*S*/3*R* started to decrease after 2 h, while the peaks corresponding to 1*S*/1*R* increased. Finally, the peaks corresponding to 2*S*/2*R* appeared after 3h. On the other hand, (*S*-4BrMBA)$_4$AgBiBr$_8$ thin films show a slightly slower evolution toward polymorphism (Figures S20 and S21, Supporting Information). The long-term stability of the thin films was confirmed since the XRPD patterns were unchanged after one month. On the other hand, the thin films have been exposed to a second annealing step by heating at 95 °C

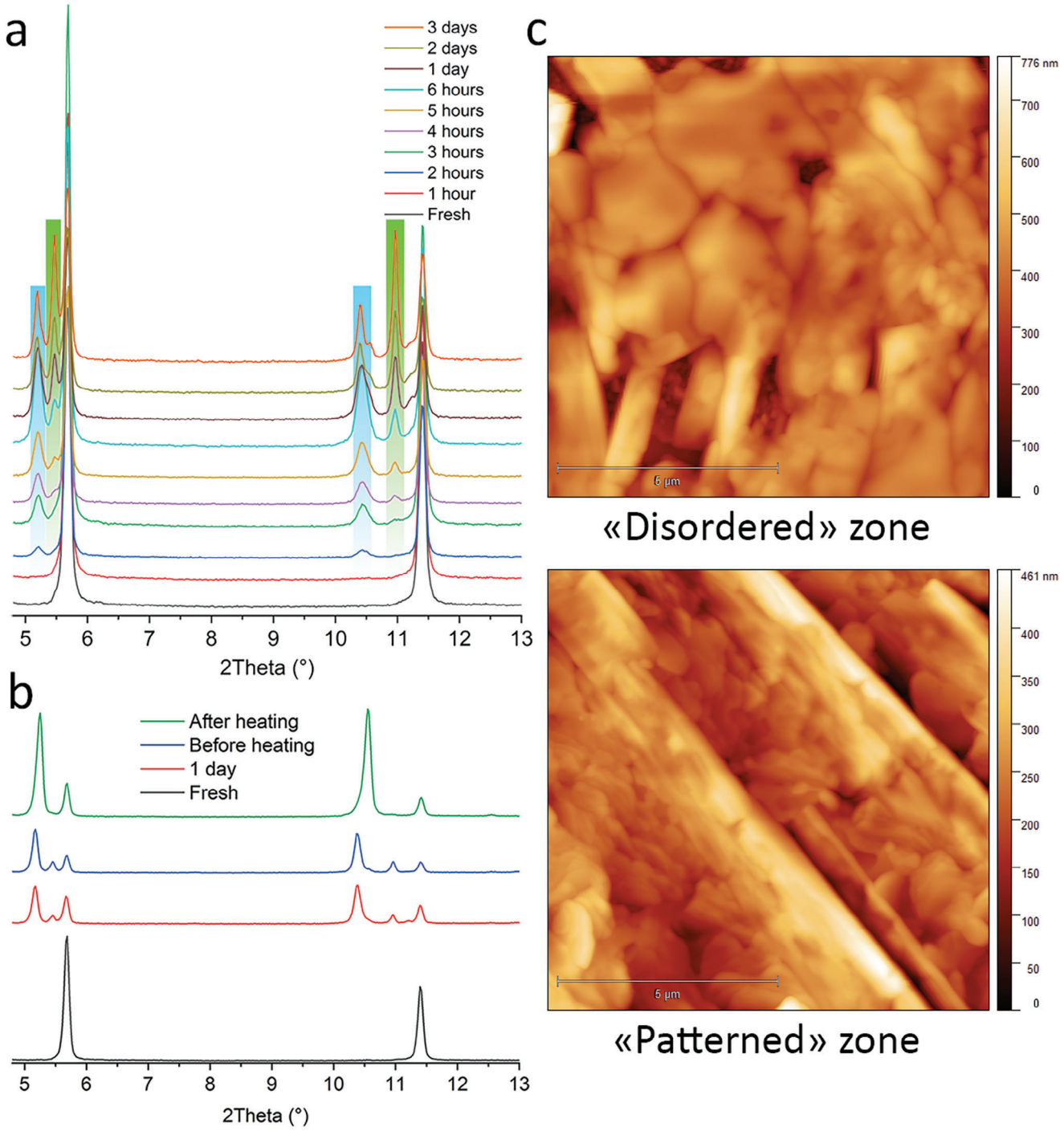

Figure 3. Characterization of $(R\text{-4BrMBA})_4AgBiBr_8$ thin film prepared from a precursor solution at c = 0.5 M. a) Time-resolved XRPD study showing the appearance of the two phases associated to the bulk triclinic (highlighted in blue) and orthorhombic phases (in green). b) Evolution of the XRPD of the aged film after heating at 95 °C for 10 min. c) AFM topography images showing the two distinct zones observed in the thin film.

for ≈10 min. A drastic change in the XRPD pattern could be observed (Figures 3b; Figure S22, Supporting Information). Indeed, the peaks associated to $2S/2R$ vanished and have been replaced by the peaks associated to $1S/1R$. This last series of measurements also suggested that polymorphs $3S$ and $3R$ are not solvates since these ones didn't vanish upon heating. It is thus reasonable to believe that $3S/3R$ is a thermodynamically unfavored 2D polymorph which could only be obtained thanks to the energy provided during the annealing step. From a structural point of view, the evolution of the XRPD patterns can be understood on the basis of tunable stacking of the 2D organic and inorganic layers in the hybrid compounds. Indeed, the composition of the

film changed from closely stacked 2D layers with an interlayer distance d = 15.5 Å (2Theta = 5.69°) to a mixture with the orthorhombic and triclinic phases in which interlayer distances increased up to d = 16.1 and d = 16.9 Å (2Theta = 5.46 and 5.23°), respectively. Therefore, the evolution of the thin films can be seen as a "breathing" of the 2D layered perovskite network. Finally, atomic force microscopy (AFM) measurements were performed on various zone of the aged film and reveal two distinct patterns (Figure 3c). A first zone of strong disorder with random orientation of flakes seemed to support the polymorphism inside the thin film. However, a second zone revealed a better organized pattern which may be the result of an oriented crystallization. Both types of zones presented similar roughness and maximum height (Figure S23, Supporting Information).

On the other hand, thin films of $(S/R\text{-4BrMBA})_4AgBiI_8$ didn't show any phase transition, as highlighted by the presence of the expected peaks corresponding to (001) and (002) planes for all thicknesses (Figure S24, Supporting Information), and no further evolution upon aging (**Figure 4a**). As observed during the single-crystal structure characterization, the presence of iodine anions in the inorganic layer induced only one type of cation-anion interaction and one type of organization for the organic layer, at the difference of the smaller bromide anion which may result in higher constraints for the organic part, as illustrated by the two independent organic layers in $1S/1R$ with very different organization of the cations. Combining these results, it is envisaged that such competition between different cation-anion interactions in the bromide-based compounds could favor the transformation in the organic layer and be at the origin of the polymorphism. Optical microscopy images revealed the presence of domains separated by grain boundaries, with bright and dark spots suggesting zones of different thicknesses (Figure 4b). This was further confirmed by AFM measurements. Topography images on dark zones revealed a very smooth surface of the thin film, with a small overall roughness determined at ≈10 nm (Figure 4c; Figures S25 and S26, Supporting Information). On the other hand, the deposition of a very thin layer of the 2D compound in the bright zone was demonstrated by its texture and higher roughness, similar to the one of the FTO substrate (Figure S27, Supporting Information). In addition, a very regular stripped pattern was observed in both types of zones, suggesting the highly oriented deposition and crystallization of the 2D material.

2.4. Evolution of the Chiroptical Properties in the Thin Films

CD in highly crystalline thin films such as chiral metal-halide networks can be easily modulated by the interference between linear dichroism (LD) and linear birefringence (LB). In addition to the real thickness-independent molecular CD_{iso} term, it was recently demonstrated that these macroscopic effects could give rise to additional thickness-dependent signals called aLDLB (where "a" stands for "antisymmetric" due to the change in sign of the associated signal upon sample flipping)[26] and sLDLB ("symmetric" effect which is not affected by the position of the film during the analysis).[27] Given the strong evolution of the crystal phases in $(S/R\text{-4BrMBA})_4AgBiBr_8$ thin films, a careful analysis of the CD response has been undertaken, by analyzing first the CD of the freshly prepared thin films and further measuring one day after fabrication. In addition, the absence of a main polar axis in these non-polar crystalline compounds suggest substantial LB and therefore, possible aLDLB and/or sLDLB effects.[28] Regarding the fresh films prepared from a precursor solution at c = 0.3 M, no change in the CD signal could be observed by turning over an azimuth angle of 90°, thus confirming the absence of artefacts (Figure S28, Supporting Information). To disclose between molecular and macroscopic origins of the observed CD signals, another set of measurements were performed after flipping the thin film inside the CD spectrometer, the "front" and "back" configurations corresponding to the perovskite film oriented toward the light source and the detector, respectively (Figure S28, Supporting Information). Since aLBLD change sign upon sample flipping, both CD_{iso} and aLDLB contributions can be calculated from the experimental "front" and "back" spectra using the equations: $CD_{iso} = ½ (CD_{front} + CD_{back})$ and $aLDLB = ½ (CD_{front} - CD_{back})$.[29] The same signal observed between "front" and "back" measurements in the fresh films confirmed that the CD signals are dominated by reciprocal circular absorption due to intrinsic chirality in the hybrid compound, with absence of macroscopic effects such as aLDLB (**Figure 5a**). This is also confirmed by the very weak LD signal measured at all positions (Figure S29, Supporting Information). In addition, absorbance spectra are typical of a 2D $AgBiBr_8$ network with an excitonic band centered at 390 nm, which strongly support the nature of the polymorph $3S/3R$. We can conclude at this step that $(S\text{-4BrMBA})_4AgBiBr_8$ and $(R\text{-4BrMBA})_4AgBiBr_8$ thin films present a continuous positive and negative CD signal, respectively, with a g_{abs} of $\approx\pm3.10^{-4}$. Very surprisingly, the same films presented a completely different behavior after one-day ageing. Indeed, the appearance of a LD signal could now be observed, with a clear $\sin 2\theta$ periodicity (Figure S30, Supporting Information). At the consequence, aLDLB strongly affected the CD signal. The almost mirror-image spectra observed between "front" and "back" measurements for a same enantiomer highlighted the dominance of these macroscopic effects in the chiroptical properties of the aged films (Figure S31, Supporting Information). The relatively strong signals obtained for aLDLB confirmed the presence of macroscopic anisotropy (Figure 5b). This can be understood based on the multiple crystal polymorphs present in the thin film, which results in the non-homogeneous deposition. The CD_{iso} and aLDLB spectra show no exact mirror-image signals between S and R enantiomers, which can be understood based on the slightly different aging of the thin films, as highlighted by the XRPD evolution (vide supra). For the same reasons, the CD signal in the aged films can vary from batch to batch for a same enantiomer, although the CD measured on fresh films was always consistent in all our experiments, even when starting from a different batch of crystals. Such modulation in the aged films was expected since chiroptical properties is usually affected by very small structural differences or traces of impurities. More surprisingly, the calculated CD_{iso} signal, which represents the chiroptical behavior of the compound in its ground state, shows an inversion of the signal compared to the CD of the fresh film for the same enantiomer. Indeed, $(S\text{-4BrMBA})_4AgBiBr_8$ now presents a continuous negative CD signal in the entire region of absorbance of the inorganic network. Considering the increasing distance between inorganic layers in the orthorhombic and triclinic phases compared to the first phase (as illustrated

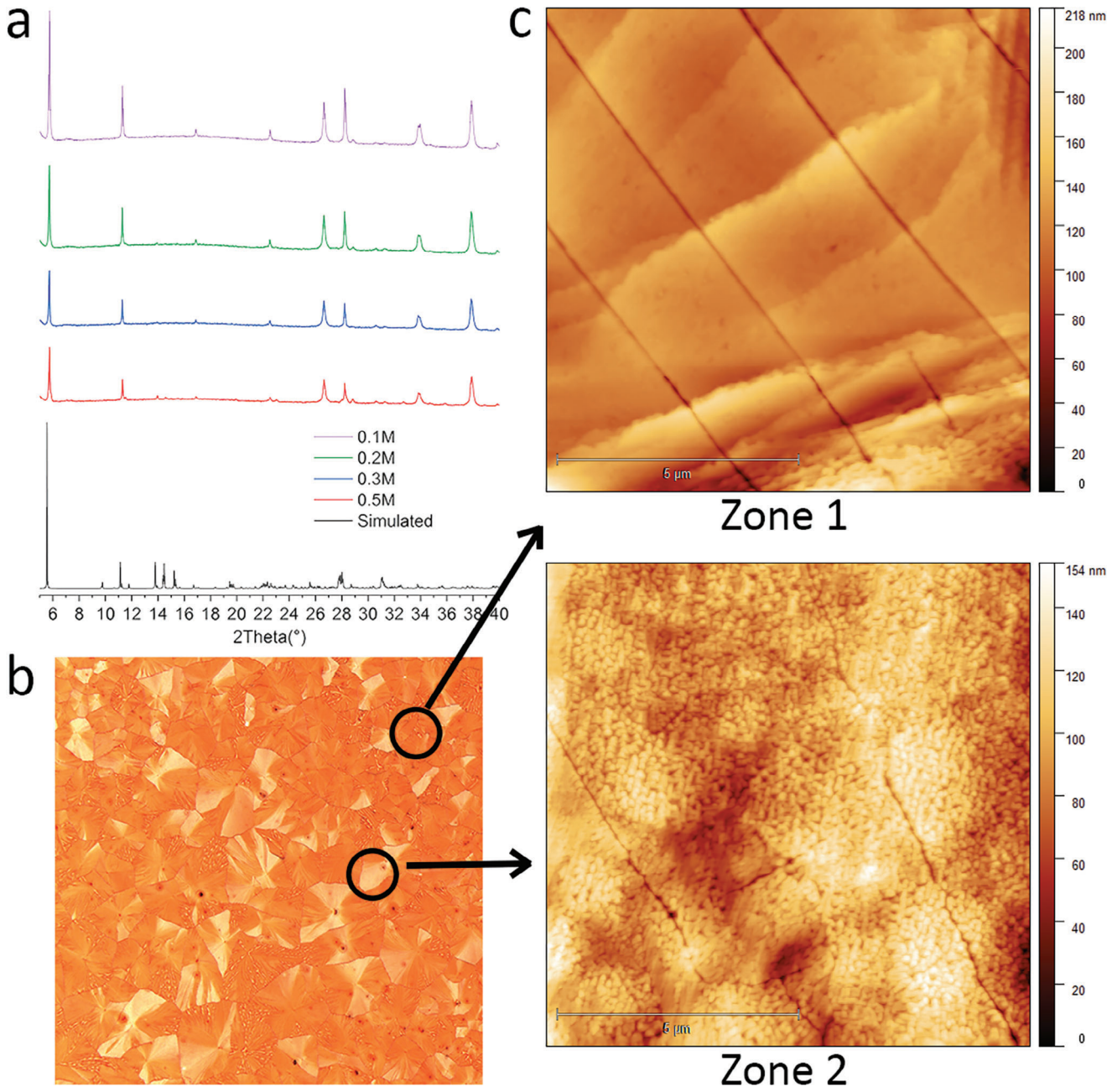

Figure 4. Characterization of $(R\text{-4BrMBA})_4AgBiI_8$ thin films. a) Simulated and experimental XRPD patterns for thin films of different thicknesses after one-day aging. The three peaks at 2Theta = 26.6, 33.8, and 37.8° correspond to the FTO substrate. b) 2 × 2 mm optical microscopy image of the thin film prepared from a precursor solution at $c = 0.5$ M. c) AFM topography images of the thin film, showing the smooth surface in the zone of strongest deposition of material (zone 1) and the more textured surface in the zone of lower deposition (zone 2).

by XRPD), a small variation in CD_{iso} between fresh and aged films could be expected. However, a complete change in sign suggests a strong structural modulation in the geometry of the metal-halide anions between polymorphs. Similar results were obtained for the different film thicknesses (Figures S32 and S33, Supporting Information). The linear evolution of both CD and absorbance gives rise to an almost constant value of g_{abs} (Figures S34 and S35, Supporting Information), therefore no symmetric LDLB (sLDLB) effects could modulate the chiroptical properties of the bromide-based networks. It should be noted that for the lowest concentration of 0.1 M, the same change in sign of CD_{iso} was observed but at the same time no aLDLB was affecting the CD response on the aged film (as highlighted by the very similar "front" and "back" measurements, see Figure S33, Supporting Information), therefore the calculated CD_{iso} in the whole series seem to correspond to the true chirality of the hybrid compound, and discard the possible wrong estimation of CD_{iso} by averaging "front" and "back" measurements. Finally, the CD signal was

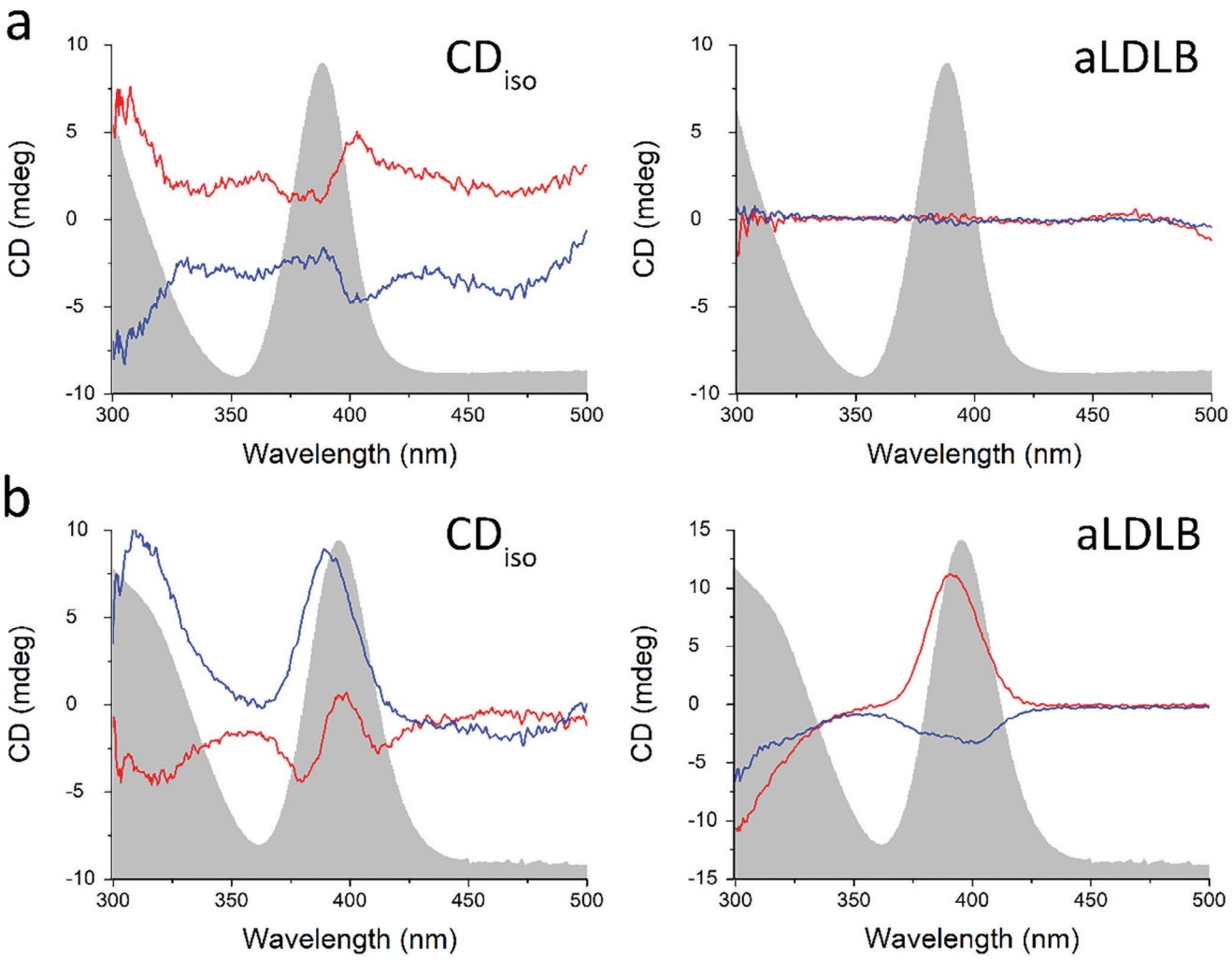

Figure 5. Absorption (grey area) and CD characterization of (*S*-4BrMBA)$_4$AgBiBr$_8$ (red lines) and (*R*-4BrMBA)$_4$AgBiBr$_8$ (blue lines). a) CD$_{iso}$ and aLDLB for the freshly prepared thin films. b) CD$_{iso}$ and aLDLB for the same thin films after one day.

not affected by the second annealing on the thin films, despite the substantial changes observed in XRPD (vide supra).

Such a strong modulation of the CD signature was not observed in the thin films of (*S*/*R*-4BrMBA)$_4$AgBiI$_8$. Such as XRPD measurements, for which no phase transition could be observed, CD measurements show no difference between fresh and aged films. As for the bromide-based compounds, no differences could be observed depending on the azimuth angle θ, confirming the absence of artefacts (Figure S36, Supporting Information). However, strong differences could be observed between "front" and "back" measurements, revealing the presence of a strong aLDLB effect in (*S*/*R*-4BrMBA)$_4$AgBiI$_8$ thin films, with an amplitude similar to the CD$_{iso}$ signal (**Figure 6**). It should be noted that the calculated CD$_{iso}$ and especially aLDLB spectra show no exact mirror-image response between (*S*-4BrMBA)$_4$AgBiI$_8$ and (*R*-4BrMBA)$_4$AgBiI$_8$. Although starting from the same concentration of the precursor solution (c = 0.5 M) for both *S* and *R* enantiomers, the resulting thin films present a slight difference in film thickness (as highlighted by the small difference in total absorbance values). Given the large amplitude in the CD modulation by increasing film thickness in iodide-based compounds (Figure S37, Supporting Information), we can explain such difference in CD$_{iso}$ and aLDLB between enantiomers based on this small thickness variation. Finally, the increasing CD response by increasing film thickness is confirmed by the strong evolution of g_{abs} calculated from the CD$_{iso}$ spectra at each concentration (Figure S38, Supporting Information). Indeed, it was calculated the highest $g_{abs} = \pm 3.10^{-3}$ in the film prepared from a precursor solution at c = 0.5 M. These values decrease down to $g_{abs} = \pm 3.10^{-4}$ for the thinnest films that we were able to prepare and characterize. These results suggest the presence of sLDLB due to the twist angle in the helical stacking of 2D layers, leading to a thickness-dependent CD signal.

In conclusion, CD$_{iso}$ is of the same intensity in both bromide and iodide-based networks, but the CD response is strongly modulated by macroscopic anisotropy. To the best of our knowledge, such behavior has been so far observed in 1D or 0D metal-halide compounds, while 2D networks based on divalent metals usually

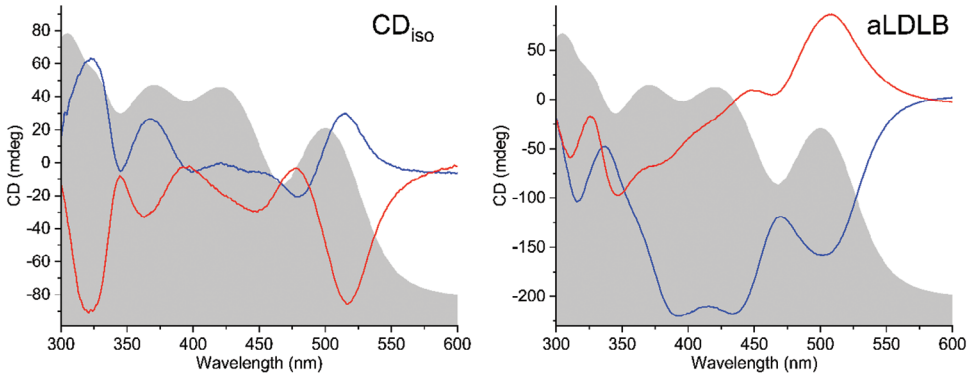

Figure 6. Absorption (grey area) and CD characterization of (*S*/*R*-4BrMBA)$_4$AgBiI$_8$ thin films prepared from a precursor solution at $c = 0.5$ M.

present very low CD signals with no macroscopic effects.[26] The strongest distortion of the octahedra in 2D double perovskites may contribute to the increasing CD response in the series of thin films here studied. In addition, the presence of polymorphism and crystal domains result in a predominant contribution of aLDLB in the CD signal of (*S*/*R*-4BrMBA)$_4$AgBiBr$_8$ compared to the CD$_{iso}$ term. On the other hand, both aLDLB and sLDLB are present in the thin films of *S*/*R*-4BrMBA)$_4$AgBiI$_8$. CD$_{iso}$ and aLDLB have comparable contribution in the experimental signals, while sLDLB leads to a more dramatic increase of the CD signal compared to bromide-based compounds, increasing the calculated dissymmetry factors by one order of magnitude in the range of film thickness here studied. As observed previously in 1D metal-halide networks,[27] this behavior can be explained based on a more homogeneous deposition of a single-phase material in (*S*/*R*-4BrMBA)$_4$AgBiI$_8$.

3. Conclusion

A rare series of chiral double perovskites of general formula (*S*/*R*-4BrMBA)$_4$AgBiX$_8$ is here presented. The challenge to synthesize this type of hybrid compounds have been overcome by selecting both a suitable chiral organic cation and the synthetic conditions to avoid the formation of discrete monometallic species such as BiX_5^{2-} salts. While the iodide-based perovskites presented only one crystal structure, their bromide-based counterparts show polymorphism with the characterization of two crystal structures with different symmetries. The triclinic phase has the particularity to present two different organic or inorganic layers in the asymmetric unit as highlighted by the very different arrangement of chiral cations between the two organic layers. On the other hand, the orthorhombic phase presents a large periodicity leading to a wavy structure. Such polymorphism was also found at the nanoscale, since the thin films prepared from a polycrystalline sample of (*S*/*R*-4BrMBA)$_4$AgBiBr$_8$ show the presence of an undefined third crystal phase of the same 2D compound, according to XRPD. Surprisingly, the thin films evolve in the first hours to finally result in a mixture of the three crystal phases. This modulation of the film structure results in a strong evolution of the CD signals, from a small CD$_{iso}$ with a g_{abs} of $\pm 3.10^{-4}$ in the original film to a strong CD dominated by aLDLB. Finally, in (*S*/*R*-4BrMBA)$_4$AgBiI$_8$ thin films, both aLDLB and sLDLB effects could be observed, with a regular increase of g_{abs} from 3.10^{-4} to 3.10^{-3} across the range of film thickness. These results confirm the moderate strength of intrinsic CD in the family of chiral 2D (double) perovskites and highlight the predominant role of macroscopic effects in non-polar but highly anisotropic materials. Consequently, the CD signals in (*S*/*R*-4BrMBA)$_4$AgBiX$_8$ are among the highest ever observed in the family of 2D halide perovskites, probably due to the stronger distortion of the inorganic networks based on Ag^+/Bi^{3+} compared to Pb^{2+} or Sn^{2+}. We are currently investigating the CISS effect in this series of thin films, in order to reveal the effect of both the nature of metal and halide ions and of the CD strength on the spin-polarization ability of low-dimensional halide perovskite materials.

4. Experimental Section

Materials and Methods: Hydrobromic acid (48 wt % in H_2O), hydroiodic acid (57 wt % in H_2O, distilled, stabilized, 99.95%), hypophosphorous acid solution (50 wt % in H_2O), ethanol (96%), $BiBr_3$ (98%), $Bi(NO_3)_3{\cdot}5H_2O$ (98%), $AgNO_3$ (99%), (*R*)-(-)-1-(phenyl)ethylamine (98%), (*S*)-(-)-1-(4-Bromophenyl)ethylamine (98%) and (*R*)-(+)-1-(4-Bromophenyl)ethylamine (98%) were purchased from commercial sources and used as received, without further purification.

Synthesis: *Synthesis of (S-4BrMBA)$_4$AgBiBr$_8$ and (R-4BrMBA)$_4$AgBiBr$_8$*: 0.5 mmol $AgNO_3$ (84.9 mg) was dissolved in 5 mL of HBr under magnetic stirring and heating at 200 °C. The vial was then covered with a glass substrate. After 10 min the solution turned into dark red due to the oxidation of Br^- to Br_2 induced by $AgNO_3$. 12 drops of H_3PO_2 acid were added to the solution in order to reduce Br_2, turning the solution into clear yellow. Then, 0.5 mmol of $BiBr_3$ (224 mg) was added to the solution. After dissolution, the temperature of the hot plate was set to 150 °C. 1 mmol of *S*/*R*-4BrMBA ($V = 146.9$ µL) was added along with nine drops of ethanol. After 3 min, the hot plate was turned off and the solution was left to cool down to room temperature. Yellow plate-like crystals started to form after a few minutes and within 1 hour the crystals precipitated. The product was filtrated and left to dry for a day. Yield: 242 mg (28%) for both enantiomers. The high temperature phase of these compounds was obtained by heating the product in an oven at 120 °C for 30 min.

Synthesis of (S-4BrMBA)$_4$AgBiI$_8$ and (R-4BrMBA)$_4$AgBiI$_8$: 0.25 mmol of $Bi(NO_3)_3{\cdot}5H_2O$ (121.3 mg) and 1 mmol of $AgNO_3$ (169.8 mg) were dissolved in 6 mL of HI under stirring and heating at 120 °C for 10 min. In a separate vial, 1 mmol of *S*/*R*-4BrMBA ($V = 146.9$ µL) was added to 1 mL of H_3PO_2 solution under stirring at room temperature. The neutralized *S*/*R*-4BrMBA was then added to the HI solution under heating and stirring until a clear red solution was obtained. The temperature was lowered

to 60 °C until red plate-like crystals precipitated. The solution was cooled to room temperature until the product fully precipitated. The red crystals were filtrated and left to dry for a day. Yield: 194 mg (36%) and 271 mg (50%) for (*S*-4BrMBA)$_4$AgBiI$_8$ and (*R*-4BrMBA)$_4$AgBiI$_8$, respectively.

Synthesis of (R-MBA)$_2$BiBr$_5$: This compound was prepared in a similar manner to **(*S*/*R*-4BrMBA)$_4$AgBiBr$_8$** starting from *R*-MBA instead of *S*/*R*-4BrMBA, leading in that case to large prismatic red crystals. Yield: 273 mg (64%).

Synthesis of (R-MBA)$_2$BiI$_5$: This compound was prepared in a similar manner to **(*S*/*R*-4BrMBA)$_4$AgBiI$_8$** starting from *R*-MBA instead of *S*/*R*-4BrMBA, leading in that case to large prismatic red crystals. Yield: 290 mg (68%).

Thin Films Preparation: 15 × 15 mm FTO substrates were subsequently washed by ultrasonication in soap water and ethanol and further dried under N2 flow. The precursor solutions were prepared by dissolving crystals of the compounds in anhydrous DMF. 50 µL of the solution was deposited on the FTO substrate and spin coating was performed at 1000 rpm (10 s) and 6000 rpm (20 s). The films were placed on a 95 °C hot plate during 10 min for annealing.

X-Ray Structure Determinations: X-ray diffraction data were collected on a Rigaku Oxford Diffraction SuperNova diffractometer equipped with Atlas CCD detector and micro-focus Cu-K$_\alpha$ radiation ($\lambda = 1.54184$ Å). Data were collected at 200K for both enantiomers of (4BrMBA)$_4$AgBiBr$_8$ and at room temperature for both enantiomers of (4BrMBA)$_4$AgBiI$_8$. Intensities were corrected for Lorentz-polarization effects, as well as for absorption effect (gaussian method using CrysAlisPro program -CrysAlisPro, Rigaku Oxford Diffraction, V1.171.41.118a, 2021). Crystal structures were solved by charge flipping and refined (full-matrix least-squares on F^2) using the Jana2006 package. CCDC 2382693 ((*S*-4BrMBA)$_4$AgBiBr$_8$ triclinic), CCDC 2382694 ((*R*-4BrMBA)$_4$AgBiBr$_8$ triclinic), CCDC 2382695 ((*S*-4BrMBA)$_4$AgBiBr$_8$ orthorhombic), CCDC 2382696 ((*R*-4BrMBA)$_4$AgBiBr$_8$ orthorhombic), CCDC 2382697 ((*S*-4BrMBA)$_4$AgBiI$_8$) and CCDC 2382698 ((*R*-4BrMBA)$_4$AgBiI$_8$) contain the supplementary crystallographic data for this paper. This data can be obtained free of charge from The Cambridge Crystallographic Data Centre via www.ccdc.cam.ac.uk/data_request/cif. Crystallographic data of all compounds are summarized in Tables S1–S6 (Supporting Information). A Bruker D8 ADVANCE was used to analyze the powder and film patterns of the synthesized compounds. It is mounted in the Bragg-Brentano geometry in θ-2θ measurement. The X-rays were formed by a copper anti-cathode of wavelength 1.5406 Å allowing to obtain a diffractogram of $I = f(2\theta)$. The detection angles started from 5^0 up to 40^0.

Thermal Analysis: Thermogravimetric analysis (TGA). A full set of data were adopted by using a NETZSCH TG 209F3 TGA instrument. For all samples, data were collected in a temperature range of 35 to 1000 °C with a heating rate of 10 °C min^{-1}. Differential Scanning Calorimetry (DSC). A full set of data was collected by using a NETZSCH DSC 3500 instrument. Approximately 5 mg of each sample were placed in alumina crucibles under nitrogen atmosphere. Then, they were placed in the calorimeter along with an empty reference alumina crucible. The samples were first maintained in a 2 min isothermal state and then heated from −30 °C up to 160 °C and back to −30 °C with a rate of 10 °C min^{-1}.

AFM: Atomic force microscopy (AFM) experiments were performed using the Nano-Observer device (CSInstrument, Les Ulis, France). The topographic images were obtained at room temperature in contact mode using FORTA SPM Probe (AppNano, USA). Images were processed with the Gwyddion free SPM data analysis software (v2.66, Czech Metrology Institute, Brno, Czech Republic).

CD Measurements: UV–vis absorption, CD, and LD spectra were recorded in transmission mode on a JASCO J-1500 spectrometer at 20 °C. For each sample, at least eight scans were performed, at four different angles for both "front" and "back" configuration.

Supporting Information

Supporting Information is available from the Wiley Online Library or from the author.

Acknowledgements

This work was supported by the CNRS, the University of Angers and the project "*Etoiles Montantes*" from *Région Pays la Loire* (CHAOS project, postdoctoral grant to K.T.).

Conflict of Interest

The authors declare no conflict of interest.

Data Availability Statement

The data that support the findings of this study are available from the corresponding author upon reasonable request.

Keywords

chiral perovskites, chiroptical properties, circular dichroism, double perovskites, lead-free

Received: October 31, 2024
Published online:

[1] R. Naaman, Y. Paltiel, D. H. Waldeck, *Nat. Rev. Chem.* **2019**, *3*, 250.
[2] G. Long, R. Sabatani, M. I. Saidaminov, G. Lakhwani, A. Rasmita, X. Liu, E. H. Sargent, W. Gao, *Nat. Rev. Mater.* **2020**, *5*, 423.
[3] H. Lu, Z. V. Vardeny, M. C. Beard, *Nat. Rev. Chem.* **2022**, *6*, 470.
[4] S. Ma, J. Ahn, J. Moon, *Adv. Mater.* **2021**, *33*, 2005760.
[5] C. Yuan, X. Li, S. Semin, Y. Feng, T. Rasing, J. Xu, *Nano Lett.* **2018**, *18*, 5411.
[6] S. Liu, M. Kepenekian, S. Bodnar, S. Feldmann, M. W. Heindl, N. Fehn, J. Zerhoch, A. Shcherbakov, A. Pöthig, Y. Li, U. W. Paetzold, A. Kartouzian, I. D. Sharp, C. Katan, J. Even, F. Deschler, *Sci. Adv.* **2023**, *9*, eadh5083.
[7] Y. Peng, X. Liu, L. Li, Y. Yao, H. Ye, X. Shang, X. Chen, J. Luo, *J. Am. Chem. Soc.* **2021**, *143*, 14077.
[8] Y.-H. Kim, Y. Zhai, H. Lu, X. Pan, C. Xiao, E. A. Gaulding, S. P. Harvey, J. J. Berry, Z. V. Vardeny, J. M. Luther, M. C. Beard, *Science* **2021**, *371*, 1129.
[9] H. Lu, J. Wang, C. Xiao, X. Pan, X. Chen, R. Brunecky, J. J. Berry, K. Zhu, M. C. Beard, Z. V. Vardeny, *Sci. Adv.* **2019**, *5*, eaay0571.
[10] A. Abhervé, N. Mercier, A. Kumar, T. K. Das, J. Even, C. Katan, M. Kepenekian, *Adv. Mater.* **2023**, *35*, 2305784.
[11] H. Lu, C. Xiao, R. Song, T. Li, A. E. Maughan, A. Levin, R. Brunecky, J. J. Berry, D. B. Mitzi, V. Blum, M. C. Beard, *J. Am. Chem. Soc.* **2020**, *142*, 13030.
[12] C. Coccia, M. Morana, A. Mahata, W. Kaiser, M. Moroni, B. Albini, P. Galinetto, G. Folpini, C. Milanese, A. Porta, E. Mosconi, A. Petrozza, F. De Angelis, L. Malavasi, *Angew. Chem., Int. Ed.* **2024**, *63*, 202318557.
[13] Y. Zhao, M. Dong, J. Feng, J. Zhao, Y. Guo, Y. Fu, H. Gao, J. Yang, L. Jiang, Y. Wu, *Adv. Opt. Mater.* **2022**, *10*, 2102227.
[14] Z. Yu, S. Cao, Y. Zhao, Y. Guo, M. Dong, Y. Fu, J. Zhao, J. Yang, L. Jiang, Y. Wu, *ACS Appl. Mater. Interfaces* **2022**, *14*, 39451.
[15] Z. Li, C. Ji, Y. Fan, T. Zhu, S. You, J. Wu, R. Li, Z.-K. Zhu, P. Yu, X. Kuang, J. Luo, *J. Am. Chem. Soc.* **2023**, *145*, 25134.
[16] T. Zhu, X. Li, P. Yu, Z. Zhu, M. Li, R. Li, S. Han, H. Ye, C. Ji, J. Luo, *Chem* **2024**, *10*, 882.
[17] M. K. Jana, R. Song, Y. Xie, R. Zhao, P. C. Sercel, V. Blum, D. B. Mitzi, *Nat. Commun.* **2021**, *12*, 4982.

[18] J.-T. Lin, D.-G. Chen, L.-S. Yang, T.-C. Lin, Y.-H. Liu, Y.-C. Chao, P.-T. Chou, C.-W. Chiu, *Angew. Chem., Int. Ed.* **2021**, *60*, 21434.
[19] Y. Qin, F.-F. Gao, S. Qian, T.-M. Guo, Y.-J. Gong, Z.-G. Li, G.-D. Su, Y. Gao, W. Li, C. Jiang, P. Lu, X.-H. Bu, *ACS Nano* **2022**, *16*, 3221.
[20] Q. Guan, H. Ye, T. Zhu, X. Zhang, S. You, J. Wu, Y. Zheng, X. Liu, J. Luo, *Adv. Opt. Mater.* **2023**, *11*, 2202726.
[21] P.-J. Huang, K. Taniguchi, M. Shigefuji, T. Kobayashi, M. Matsubara, T. Sasagawa, H. Sato, H. Miyasaka, *Adv. Mater.* **2021**, *33*, 2008611.
[22] S. Jiang, P. Zhao, G. Xing, H. Kang, X. Li, T. Zhao, B. Li, T. Zhang, *Adv. Opt. Mater.* **2023**, *11*, 2203078.
[23] X. Fu, Z. Zeng, S. Jiao, X. Wang, J. Wang, Y. Jiang, W. Zheng, D. Zhang, Z. Tian, Q. Li, A. Pan, *Nano Lett.* **2023**, *23*, 606.
[24] L. Yao, Z. Zeng, C. Cai, P. Xu, H. Gu, L. Gao, J. Han, X. Zhang, X. Wang, X. Wang, A. Pan, J. Wang, W. Liang, S. Liu, C. Chen, J. Tang, *J. Am. Chem. Soc.* **2021**, *143*, 16095.
[25] a) The distortion index of the octahedra was calculated by VESTA using the following equation $\lambda_{oct} = \frac{1}{6}\sum_{n=1}^{6}[(d_n - d_0)/d_0]^2$; b) K. Momma, F. Izumi, *J. Appl. Crystallogr.* **2008**, *41*, 653.
[26] Z. Zhang, Z. Wang, H. H.-Y. Sung, I. D. Williams, Z.-G. Yu, H. Lu, *J. Am. Chem. Soc.* **2022**, *144*, 22242.
[27] A. Abhervé, *Adv. Opt. Mater.* **2024**, *12*, 2400381.
[28] T. Harada, R. Kuroda, H. Moriyama, *Chem. Phys. Lett.* **2012**, *530*, 126.
[29] G. Albano, M. Lissia, G. Pescitelli, L. A. Aronica, L. Di Bari, *Mater. Chem. Front.* **2017**, *1*, 2047.